

Modulating the Proton-Conducting Lanes in Spinel ZnMn_2O_4 through Off-Stoichiometry

Runzhi Qin, Shouxiang Ding, Chenxin Hou, Lele Liu, Yuetao Wang, Wenguang Zhao, Lu Yao, Yuanlong Shao, Ruqiang Zou, Qinghe Zhao,* Shunning Li,* and Feng Pan*

The intercalation of protons represents a notable component for energy storage in aqueous zinc-ion batteries. However, the mechanism of proton transport in metal oxide cathodes, especially related to how the cation distribution modulates the proton-conducting lanes, remains far from consensus due to the lack of suitable model materials. Here, taking spinel ZnMn_2O_4 cathode as a prototype, it is disclosed that a deficiency of one half of lattice Zn ions can triple its specific capacity at high rates, which is predominantly contributed by proton storage. This promotion can be rationalized by the emergence of facile concerted proton transport in the Zn-deficient sample, contrasting with the stoichiometric one, where proton intercalation undergoes a slow consecutive process. Furthermore, the restricted Zn motion in spinel phase causes high structural stability during cycling, preventing the recombination of external Zn ions with Zn vacant sites that readily accommodate protons. This work highlights the key role of controlled off-stoichiometry in optimizing proton transport and storage for aqueous batteries.

with more in-depth understanding of the energy storage mechanism for these cathodes, it was found that the charge carriers are not restricted to Zn ions during operation. Indeed, protons prevalently participate in the electrochemical reactions by reversibly intercalating into the cathode materials.^[12–18] Recent research has discovered that proton storage could even make up a larger proportion than Zn storage in some host materials, enabling their future use as cathodes for proton batteries.^[19,20] It is therefore tempting to explore how proton transport and storage are modified by changes in local structure of these cathodes, especially without sacrificing their high-rate and long-term performance.

Various cathode materials, including manganese oxides,^[21–25] vanadium oxides,^[26–29] Prussian blue analogues,^[30,31] and organic compounds,^[32,33] have been

demonstrated to deliver high capacity relying on $\text{H}^+/\text{Zn}^{2+}$ co-intercalation. The proton transport process therein was envisaged to go through the Grotthuss mechanism,^[34–36] similar to the way of concerted proton hopping in water—that is, when a proton is transferred between two O atoms, another proton at the designated O atom would concomitantly hop to the third O atom in the hydrogen bond network.^[37,38] This scenario of collective proton motion calls into question whether the intercalated Zn^{2+} ions can influence the topology of hydrogen bond network and the dynamics of proton transport. In our previous work, we showed that the distortion of tunnel structure in a MnO_2 electrode could modulate proton diffusion inside the bulk phase, leading to remarkably high capacity for AZIBs.^[21] Given the merits of considerable capacity, appropriate voltage and abundant resource, manganese oxide cathode materials are now a focus of attention in the research of AZIBs, but very little is known about the ways in which the local environment of their tunnel structures regulates the proton storage behavior.^[39] Moreover, it remains ambiguous whether the oxygen sublattice in these compounds, as the main contributor to the formation of hydrogen bond network, governs the extent of proton intercalation, or if there exists a close relationship between the metal cation sublattice and the overall proton storage performance.

To tackle the above issues, it is highly desirable to choose a manganese oxide with pronounced structural stability for investigation.^[40,41] Spinel-phase ZnMn_2O_4 could be taken as a model system, because it is one of the ground-state compounds in the

1. Introduction

Due to their high safety, good environmental friendliness, and competitive cost, aqueous zinc-ion batteries (AZIBs) are considered one of the most promising alternatives to lithium-ion batteries, especially in the field of stationary grid-scale energy storage.^[1–6] AZIBs employ water solution as the electrolyte, which guarantees their nonflammability, but in the meantime undermines the energy density owing to the narrow electrochemical stability window of water.^[7,8] To boost the energy density, substantial efforts have been devoted to the development of cathode materials that exhibit high capacity for Zn storage.^[9–11] However,

R. Qin, S. Ding, C. Hou, L. Liu, Y. Wang, W. Zhao, L. Yao, Q. Zhao, S. Li, F. Pan
School of Advanced Materials
Peking University
Shenzhen Graduate School
Shenzhen 518055, P. R. China
E-mail: zhaoqh@pku.edu.cn; lisen@pku.edu.cn; panfeng@pkusz.edu.cn
Y. Shao, R. Zou
School of Materials Science and Engineering
Peking University
Beijing 100871, P. R. China

 The ORCID identification number(s) for the author(s) of this article can be found under <https://doi.org/10.1002/aenm.202203915>.

DOI: 10.1002/aenm.202203915

Zn-Mn-O phase diagram and its formation is nearly inevitable after long-term electrochemical cycling of other phases of manganese oxides.^[42,43] Recently, there has been much controversy about the intrinsic performance of spinel ZnMn₂O₄ as an AZIB cathode. Some studies showed that the diffusion of cations is extremely sluggish due to high electrostatic resistance imposed by the relatively narrow tunnels in spinel structure,^[44,45] while other reports demonstrated that the spinel phase derived from transition of K⁺-pre-inserted layer-phase Zn_xMnO₂ could exhibit high capacity with outstanding rate capability and cyclability.^[46] Moreover, it was found that Mn and O deficiency in spinel ZnMn₂O₄ can promote the kinetic performance,^[40,47,48] and therefore off-stoichiometry was proposed to account for the efficiency of H⁺/Zn²⁺ co-intercalation. As we showed in our early preliminary study on this spinel-phase cathode, charge carriers are mainly protons rather than Zn²⁺, which guides us to perceive the important role of off-stoichiometry on proton conduction.^[22] A more comprehensive understanding of this impact may serve to reconcile the previous conflicting experimental results.

In this work, we perform control experiments to compare the proton storage performance between near-stoichiometric and Zn-deficient samples of spinel ZnMn₂O₄. Both samples are in situ prepared from a rapid phase evolution of the layered manganese oxide precursor in electrochemical cycling. The Zn-deficient sample, with only half of the Zn²⁺ ions remaining, displays a 33% increase in total specific capacity at 0.1C with respect to its counterpart, which is contributed by the boost in proton storage. At higher rates, such as 10C, the capacity of Zn-deficient sample can reach as high as three times that of the latter. Density functional theory (DFT) calculations further reveal the modification of proton-conducting lanes and the acceleration of proton intercalation after the removal of half of Zn ions in the 3D tunnels of ZnMn₂O₄. The off-stoichiometric cathode still demonstrates promising cyclability, indicating high stability of the defective structure that we also confirm theoretically. Together, these results inform novel defect engineering strategies to resolve the fundamental challenge of optimizing proton transport and storage in AZIB cathodes.

2. Results and Discussions

2.1. Preparation and Structural Characterization

Figure 1a shows the schematic formation process of Zn-deficient spinel ZnMn₂O₄. The precursors exhibit a flower-like morphology (Figure S1, Supporting Information) and their X-ray diffraction (XRD) profiles can be indexed to δ -MnO₂ (PDF No. 42-1317, space group of C2/m, shown in Figure S2, Supporting Information).^[49,50] δ -MnO₂ adopts a layered structure, in which Zn and K ions could be readily intercalated between the layers, as evidenced by the high-resolution transmission electron microscopy (HRTEM) images and energy-dispersive spectroscopy (EDS) results in Figure S3 (Supporting Information). Combined analysis of X-ray photoelectron spectroscopy (XPS), inductively coupled plasma optical emission spectroscopy (ICP-OES), and thermogravimetric analysis (TGA) (Figures S4, S5 and Table S1, Supporting Information) allows determination

of the compositions for precursors synthesized with and without the addition of ZnSO₄·6H₂O, and they turn out to be Zn_{0.087}K_{0.017}MnO₂·0.614H₂O and K_{0.102}MnO₂·0.424H₂O, respectively. These layer-phase precursors underwent galvanostatic discharge/charge cycling at a current density of 10C. The Zn-pre-inserted sample finally transforms into a Zn-deficient spinel, while its counterpart turns into a near-stoichiometric ZnMn₂O₄. Figure 1b provides the evolution of XRD patterns for the Zn-pre-inserted sample during cycling. The peak of (001) plane for δ -MnO₂ ($\approx 12.5^\circ$) disappears after 50 cycles, whereas the peaks at 18.9°, 33.4°, and 36.5° emerge, corresponding to the (101), (211), and (312) planes of the spinel phase. In Figure 1c,d, TEM images and electron diffraction characterization at the 800th cycle demonstrate a complete transformation into spinel phase, with uniform distribution of Zn, Mn, and O, and only trace amount of K element (Figure S6, Supporting Information). Similar observations are recorded for the K_{0.102}MnO₂·0.424H₂O counterpart, and for the precursors treated at a low current density of 1C (Figures S7–S9, Supporting Information).

The Zn to Mn elemental ratio (Zn:Mn) of the final products can be gauged from ICP-OES measurements, where the samples have been fully charged and carefully cleaned to avoid the possible byproducts. A Zn:Mn of ≈ 0.26 (Table S2, Supporting Information) is revealed for the Zn-pre-inserted sample after 800 cycles, while the corresponding value for its counterpart (without Zn pre-insertion) reaches ≈ 0.48 . This indicates that the presence of pre-inserted Zn²⁺ ions in the layered MnO₂ precursor will unexpectedly reduce the amount of remaining Zn in the charged state and facilitate the formation of Zn vacancies during structural transformation into spinel phase. According to the Zn:Mn values, we can simply refer to the Zn-deficient spinel product as Zn_{0.5}Mn₂O₄, and its near-stoichiometric counterpart as ZnMn₂O₄. The compositions can be further verified by XPS results shown in Figure 1e and Figure S10 (Supporting Information). Given that the degree of splitting between the Mn 3s peaks is inversely correlated with the valency of Mn ions,^[51,52] the difference in splitting energy between Zn_{0.5}Mn₂O₄ (4.90 eV) and ZnMn₂O₄ (5.27 eV) samples exclusively indicates higher Mn valency in the former, and hence lower Zn content. The estimated values of Mn valency are 3.44 and 3.02, respectively, in good agreement with the ICP-OES results. Raman spectra and Fourier transform infrared spectroscopy measurements also provide clear evidence of redshift of the peaks related with Mn–O stretching vibration in MnO₆ groups of Zn_{0.5}Mn₂O₄ when compared with ZnMn₂O₄ (Figure 1f and Figure S11, Supporting Information).^[53] This is consistent with the scenario of less rigid Mn–O framework in spinel structure upon the removal of Zn²⁺ ions at the tetrahedral sites, given the fact that each ZnO₄ tetrahedron is corner-shared with the MnO₆ octahedra and helps to build rigid Mn–O framework (Figure 1g).^[54]

The pre-inserted Zn²⁺ ions in the δ -MnO₂ precursor can generate an interlayer distance more suitable for Zn²⁺ diffusion, thus allowing for a much more rapid layer-to-spinel transition than that without pre-insertion (Figure 1b and Figure S7, Supporting Information).^[55] This is probably the main reason for the off-stoichiometry of the final spinel product, given the fact that too rapid reaction kinetics often leads to nonequilibrium state.^[22] We note that after the layer-to-spinel transition, the

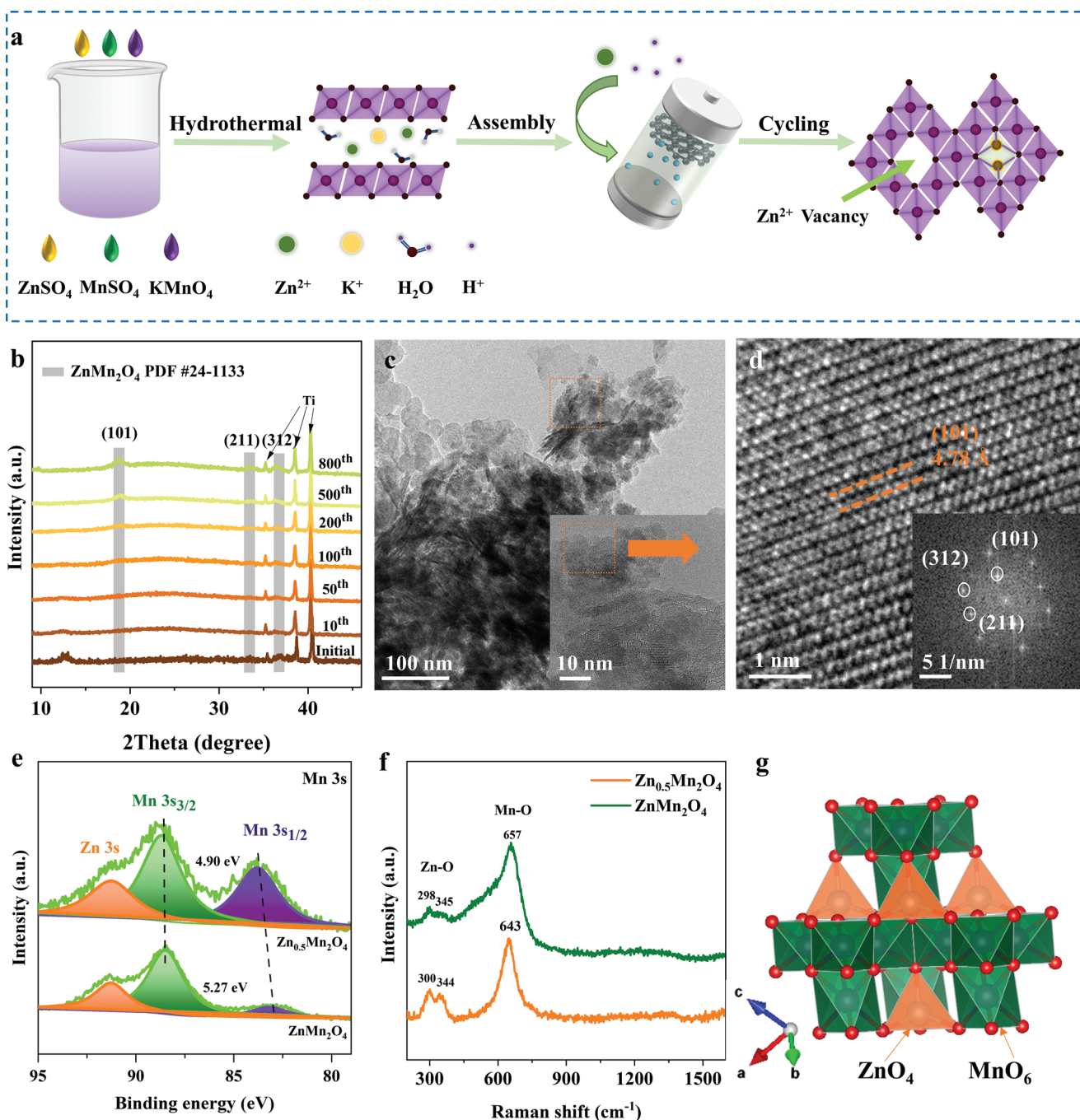


Figure 1. Material characterization of as-prepared samples. a) Schematic of synthetic path for Zn-deficient spinel ZnMn_2O_4 . b) XRD patterns of structural evolution at different electrochemical cycles for the precursor of Zn-deficient sample. c) TEM and d) HRTEM images of $\text{Zn}_{0.5}\text{Mn}_2\text{O}_4$. e) XPS spectra of Mn 3s and f) Raman spectra for $\text{Zn}_{0.5}\text{Mn}_2\text{O}_4$ and ZnMn_2O_4 . g) Crystal structure of spinel ZnMn_2O_4 and the corresponding cation-centered coordination polyhedra.

Zn content of the charged product will remain nearly constant in the following cycles, no matter if it is stoichiometric or not (Figure S12, Supporting Information). It means that the non-equilibrium state of off-stoichiometry could be stabilized once the spinel phase is formed. While the fundamental mechanism for the atomic rearrangement in this transition is still under investigation, the XRD and spectroscopic measurements could

suggest that the transition procedures are roughly identical for near-stoichiometric and Zn-deficient samples. Therefore, we can presume a close similarity between the microscopic structures of both spinel products, except for the Zn content. This establishes the rationale for our control experiments between both samples to evaluate how Zn deficiency in spinel manganese oxide affects proton transport and storage during cycling.

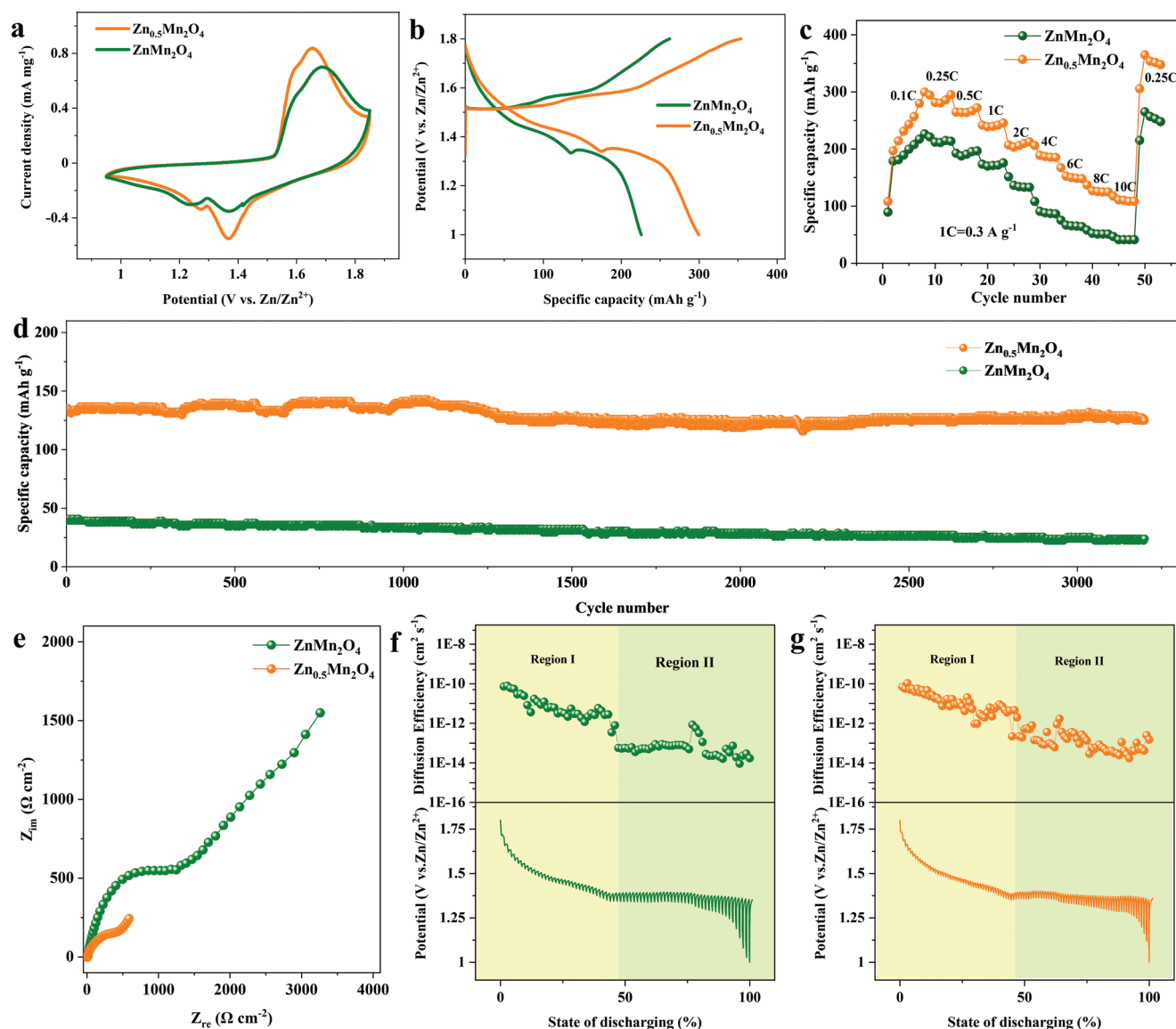


Figure 2. Electrochemical performance of Zn_{0.5}Mn₂O₄ and ZnMn₂O₄ cathodes. a) CV curves. b) Discharge–charge profiles at 0.1C. c) Rate performance. d) Cycling performance at 10C. e) EIS measurements. GITT curves and their corresponding diffusion coefficients for f) ZnMn₂O₄ and g) Zn_{0.5}Mn₂O₄ cathodes.

2.2. Electrochemical Performance

Figure 2a and Figure S13 (Supporting Information) show the cyclic voltammetry (CV) curves of Zn_{0.5}Mn₂O₄ and ZnMn₂O₄ cathodes, in which the higher peaks of the former sample indicate lower polarization and enhanced kinetics. The lower *b* values of the peak correspond to (de)intercalation- and diffusion- type behavior of charge carriers (Figure S13, Supporting Information).^[56,57] Electrochemical profiles are similar in the galvanostatic discharge/charge tests of both samples (Figure 2b), with Zn_{0.5}Mn₂O₄ delivering a specific capacity of 299.7 mAh g⁻¹ at 0.1C, and ZnMn₂O₄ delivering 225.7 mAh g⁻¹. This corresponds to 33% increase in capacity when substantial amount of Zn deficiency is introduced in the spinel cathode. Rate performance is displayed in Figure 2c, Figures S14 and S15

(Supporting Information), revealing much better capacity retention at high rates for Zn_{0.5}Mn₂O₄ than that for ZnMn₂O₄. We note that for both cathodes, while some kind of activation still takes place at low rates leading to a perceptible variation in specific capacity (similar results can be found in previous works),^[21,55] the high-rate performance barely changes in the long term, thus minimizing the possibility of significant structural reconstruction accompanying the electrochemical cycling at high rates. Especially, at 10C, a specific capacity of 135.5 mAh g⁻¹ is retained for Zn_{0.5}Mn₂O₄ (Figure 2d and Figure S16, Supporting Information), which is more than three times that of ZnMn₂O₄ (41.1 mAh g⁻¹). The sintered spinel has also been prepared, and it presents a limited capacity of only 15 mAh g⁻¹ at 1C (Figure S18, Supporting Information). Apparently, the diffusion of charge carriers is significantly promoted in

Zn-deficient sample. Moreover, for $\text{Zn}_{0.5}\text{Mn}_2\text{O}_4$ cathode, nearly 100% of the capacity is sustained for 1000 cycles, and 92% for over 3200 cycles. The discharge–charge profiles in Figure S17 (Supporting Information) demonstrate the stable polarization of the $\text{Zn}_{0.5}\text{Mn}_2\text{O}_4$ cathode. This excellent electrochemical performance has rendered it one of the most prominent materials among the manganese-oxide-based cathodes (Table S3, Supporting Information).

The promoted kinetics can be further verified by electrode impedance spectra (EIS) and galvanostatic intermittent titration technique (GITT). As shown in Figure 2e, the R_{ct} of $\text{Zn}_{0.5}\text{Mn}_2\text{O}_4$ is only $412.4 \Omega \text{ cm}^{-2}$, corresponding to about one-third that of ZnMn_2O_4 . Negligible variation of impedance is observed during cycling, indicating the stable electrochemical performance of the electrode (Figure S19, Supporting Information).^[58] The GITT results also reveal higher diffusion coefficients in both I and II regions for $\text{Zn}_{0.5}\text{Mn}_2\text{O}_4$ sample (Figure 2g) than those for ZnMn_2O_4 (Figure 2f). All the above results unequivocally confirm the superior performance of the Zn-deficient sample as compared to the near-stoichiometric one, especially in terms of rate capability, which, as will be shown below, is closely linked with the efficiency of proton transport and storage in the spinel cathodes.

2.3. Charge Storage Mechanism

Ex-situ XRD measurements were performed at 0.1C (Figure 3a,b and Figure S20, Supporting Information) for $\text{Zn}_{0.5}\text{Mn}_2\text{O}_4$ and ZnMn_2O_4 cathodes to determine their structural evolution along cycling. On discharging, pronounced peaks emerge corresponding to the byproduct $\text{Zn}_4\text{SO}_4(\text{OH})_6 \cdot 5\text{H}_2\text{O}$ (PDF No. 39-0688), while on charging, the intensities of these peaks progressively decrease and are no longer detectable at the fully charged state. The reversible formation of $\text{Zn}_4\text{SO}_4(\text{OH})_6 \cdot 5\text{H}_2\text{O}$ can also be visualized by the scanning electron microscopy (SEM) images at different discharge/charge stages (Figure 3c and Figure S21, Supporting Information), in which the large hexagonal plates indicate the appearance of this byproduct. We note that proton storage in the cathode of AZIBs will inevitably give rise to an increase in pH of the electrolyte, and the accumulation of OH^- therein will eventually lead to the formation of $\text{Zn}_4\text{SO}_4(\text{OH})_6 \cdot 5\text{H}_2\text{O}$ on the cathode surface.^[43,59,60] Therefore, the above results imply a predominance of reversible proton intercalation in $\text{Zn}_{0.5}\text{Mn}_2\text{O}_4$ and ZnMn_2O_4 . This can be further verified by the XPS O 1s spectra, which reveal a remarkable increase in the Mn-O-H peak intensity upon discharge and its subsequent decrease upon charge (Figure 3d and Figure S22, Supporting Information). It is noteworthy that no trace of H-O-H is detected in XPS spectra, meaning the absence of structural water.^[61] We can rationalize this result by considering that the spinel structure possesses relatively narrow tunnels, thus hindering the intercalation of hydronium ions and favoring the transport of single protons. The peak evolution in Mn 3s spectra corroborates the reversible redox process of Mn ions (Figure 3e), with the average valency of Mn measured to be 2.55 for $\text{Zn}_{0.5}\text{Mn}_2\text{O}_4$ cathode at its discharged state. According to the compositions of the charged and discharged products, the capacity contribution of protons and Zn^{2+} ions

can be estimated, as illustrated in Figure 3f. The proton storage accounts for over 90% of the overall capacity for both cathodes, confirming our speculation that the performance improvement upon off-stoichiometry can be mainly attributed to the modulation of dynamic proton behavior in the bulk of the cathodes.

To examine the cycling stability of the Zn-deficient sample, we resort to the ex situ XRD experiments and TEM images. The XRD patterns were collected at charged state, in which the preservation of major peaks corresponding to spinel phase is evident after operating at 10C for 3200 cycles (Figure 3g and Figure S23, Supporting Information). The absence of phase transition is consistent with previous reports on spinel manganese oxide cathodes.^[40,44] The electrode morphology after 3200 cycles is presented in Figure 3h,i and Figure S24 (Supporting Information). The interplanar spacing varies from 4.78 to 4.80 Å for the (101) facet of $\text{Zn}_{0.5}\text{Mn}_2\text{O}_4$, suggesting that there is negligible change in the lattice upon long-term cycling. The high cycling stability provides confidence that this Zn-deficient strategy could be implemented in industrial applications to boost proton storage in spinel manganese oxide cathodes for aqueous batteries.

2.4. Correlating Proton Transport and Storage with Off-Stoichiometry

The microscopic origin behind the benefits of Zn deficiency on proton transport and storage can be fully inferred from DFT calculations. To begin with, we explore the dynamics of Zn diffusion inside spinel ZnMn_2O_4 , in which interconnected Mn–O octahedra form a framework with 3D tunnels constituted by octahedral $16c$ and tetrahedral $8a$ sites. At stoichiometric composition, the $8a$ sites are fully occupied by Zn^{2+} ions, which limits the activation of their motion. Therefore, in the DFT calculations, Zn vacancies are intentionally introduced to produce vacant $8a$ sites in the tunnels. We constructed a model of $\text{Zn}_{0.875}\text{Mn}_2\text{O}_4$ to investigate Zn diffusion between neighboring $8a$ sites at near-stoichiometric compositions. For comparison, we also constructed models of $\text{Zn}_{0.5}\text{Mn}_2\text{O}_4$ and $\text{Zn}_{0.175}\text{Mn}_2\text{O}_4$ to evaluate the cases of considerable Zn deficiency and dilute Zn content. The calculated energy barriers for Zn diffusion are between 0.86 and 1.03 eV for these configurations (Figure S25, Supporting Information). Considering that the barriers of proton diffusion, as will be shown below, are significantly lower than the above values, the sluggish Zn diffusion in $\text{Zn}_x\text{Mn}_2\text{O}_4$ can be regarded as the root cause of the inferior capacity contribution of Zn^{2+} ions in electrochemical cycling. More importantly, this result can well explain the experimental observation that once the layer-to-spinel transition is completed, the Zn content of the charged product would hardly change in the following cycles, thus justifying the high structural stability of the off-stoichiometric sample.

We next evaluate the kinetics of proton transport in stoichiometric ZnMn_2O_4 . All the intercalated protons will be attached to the bridge oxygen in the tunnels, which is reminiscent of other manganese oxide cathodes for AZIBs.^[20,21,62] In stoichiometric ZnMn_2O_4 , all the oxygen sites are crystallographically equivalent, with a local coordination environment of three Mn and one Zn neighbors. Single proton hopping between two

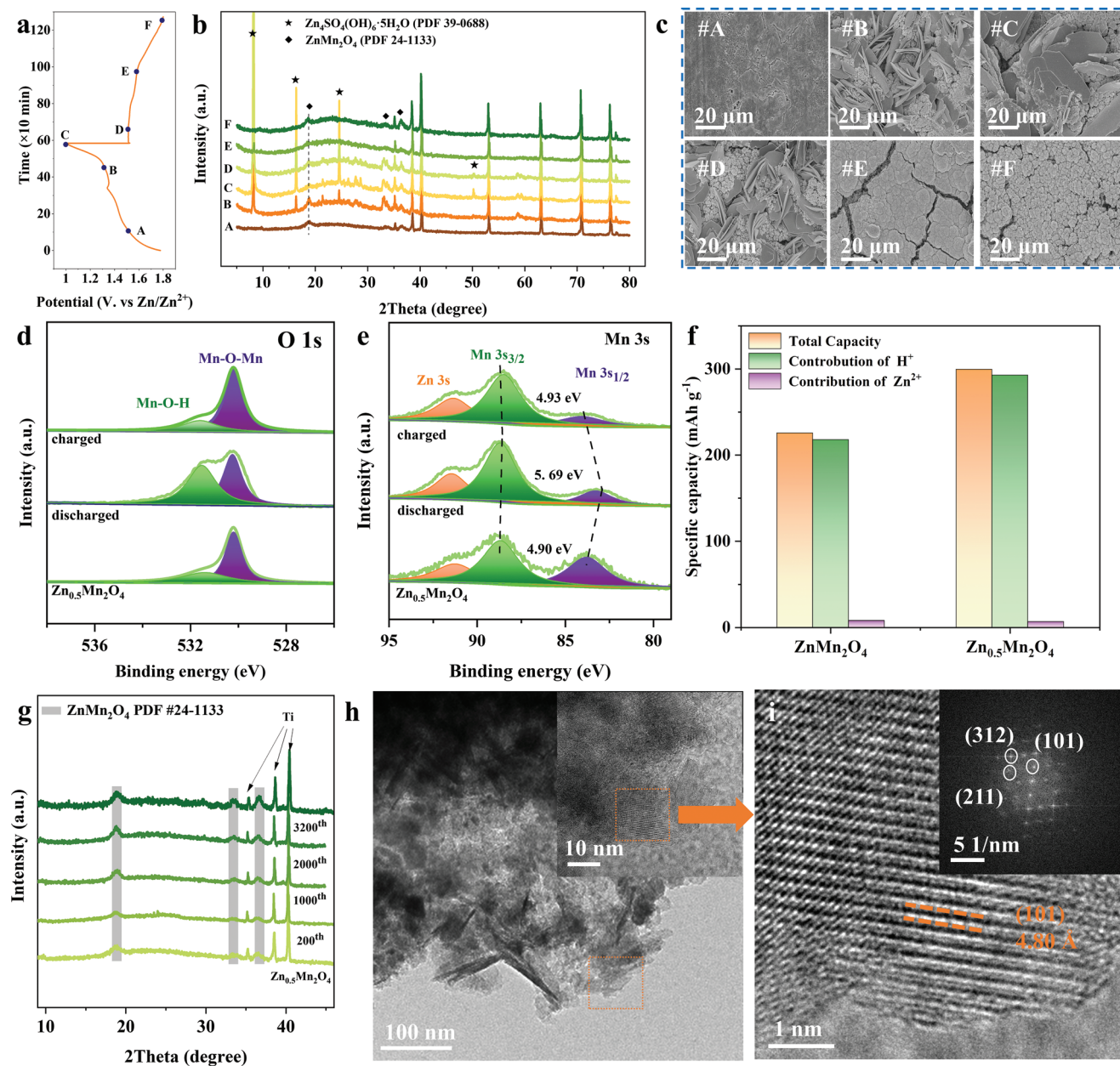


Figure 3. Charge storage mechanism of the spinel cathodes. a) Discharge–charge profiles at 0.1C, and the corresponding b) ex situ XRD patterns and c) SEM images for Zn_{0.5}Mn₂O₄. XPS spectra of d) O 1s and e) Mn 3s for Zn_{0.5}Mn₂O₄ cathode at fully discharged and charged states. f) Capacity contribution of protons and Zn²⁺ ions for Zn_{0.5}Mn₂O₄ and ZnMn₂O₄ cathodes. g) XRD patterns at different cycles for Zn_{0.5}Mn₂O₄. h) TEM and i) HRTEM images at the 3200th cycle for Zn_{0.5}Mn₂O₄.

adjacent bridge oxygen can thus be regarded as the basis for the consecutive process of proton incorporation in this spinel structure. We calculated the energy barrier for the single proton hopping process (Figure S26, Supporting Information), which is 0.77 eV, much lower than that of Zn diffusion, but higher than that of proton transport in other manganese oxides (e.g., 0.55 eV in α -MnO₂^[21]). This may account for the relatively poor rate capability of the near-stoichiometric ZnMn₂O₄ sample. However, when Zn deficiency is introduced, another kind of bridge oxygen would emerge, which has a local environment of only three Mn neighbors. As shown in Figure 4a, we

denote these two kinds of oxygen sites as O⁽¹⁾ (without Zn neighbor) and O⁽²⁾ (with Zn neighbor), respectively. The modulation of local environment of the tunnels triggers a different proton transport pattern, which confers a great mobility to the protons and allows them to cooperate with each other during hopping, leading to the excellent rate capability exhibited in the experiments.

This proton transport pattern can be described by a Grotthuss-type model along the proton-conducting lanes in Zn_{0.5}Mn₂O₄, as depicted in Figure 4b,c. At the Zn-vacant 8a site, four protons can be readily bonded to the O⁽¹⁾ atoms at this

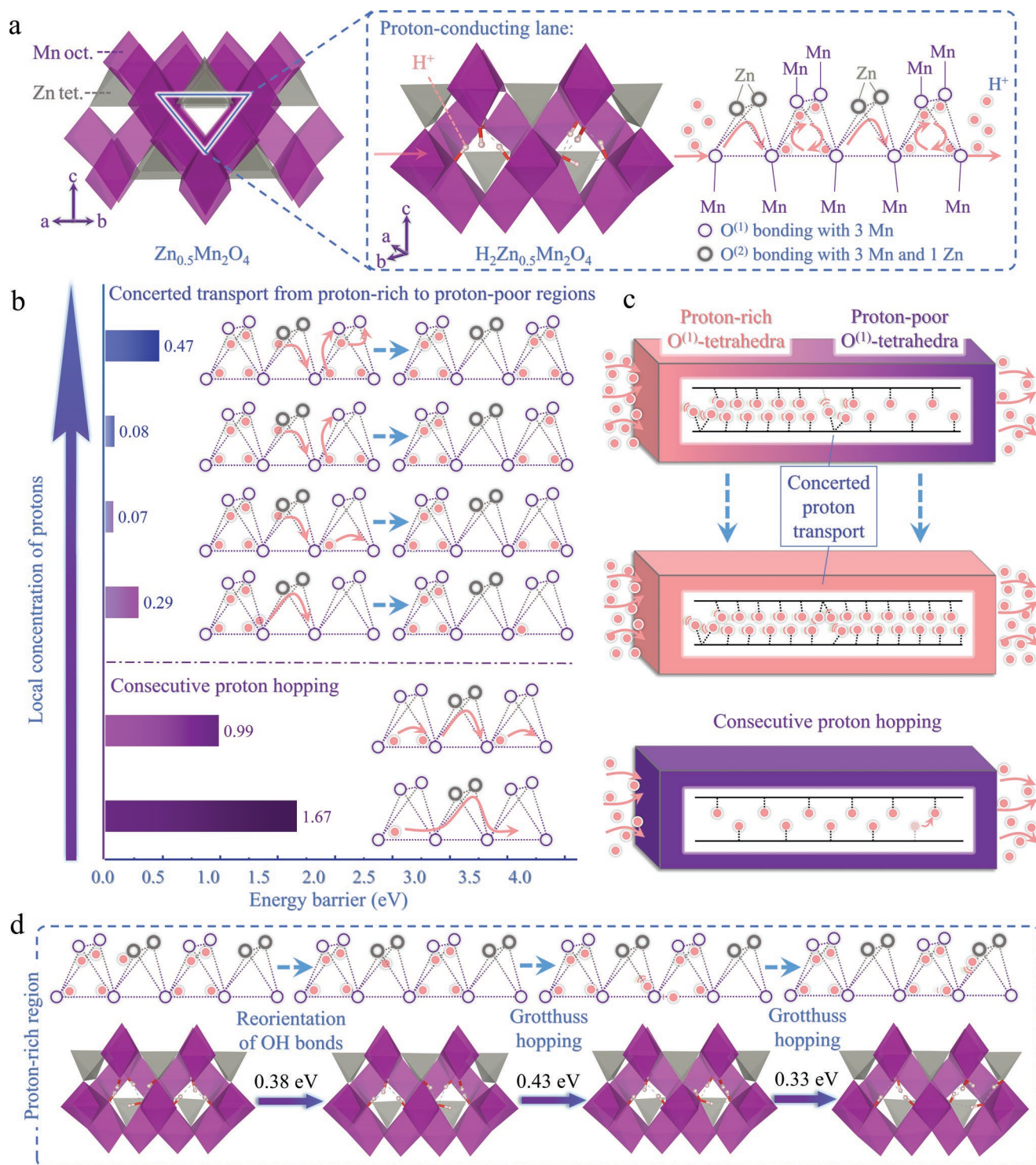


Figure 4. Theoretical calculations of proton intercalation in $Zn_{0.5}Mn_2O_4$. a) Schematic of $Zn_{0.5}Mn_2O_4$ with one half of 8a sites occupied by Zn^{2+} ions. The tunnel for proton transport is indicated, along which the protons are attached to the bridge oxygens. There are two kinds of environment for bridge oxygen, one with three Mn neighbors, denoted as $O^{(1)}$, and the other with three Mn and one Zn neighbors, denoted as $O^{(2)}$. b) Energy barriers of proton transport in different local environments characterized by proton concentration. At high local proton content, the overall dynamics of proton intercalation are dictated by the transport of protons from proton-rich region to adjacent proton-poor region. c) Two different modes of proton transport in spinel structure, i.e., the concerted transport model and the consecutive transport model. d) Concerted proton transport in the proton-rich region via Grotthuss hopping.

location, creating a proton-rich local environment that is different from the scenario in stoichiometric $ZnMn_2O_4$. The transport

of protons tends not to follow a consecutive mechanism via single proton hopping (Figure S27, Supporting Information),

but instead undergoes a concerted mechanism involving simultaneous hopping of multiple protons (Figure 4b). We consider the cases when a proton is bonded to an $O^{(2)}$ atom in the vicinity of this proton-enriched $O^{(1)}$ -tetrahedron. Due to electrostatic repulsion, the proton-enriched $O^{(1)}$ -tetrahedron enables the nearby proton at $O^{(2)}$ to easily excite into a transition state of weakly bound $-OH_2$ configuration (Figures S28–S32, Supporting Information), which subsequently de-excites into the stable $-OH$ configuration via appropriate rearrangement of the local protons. The highest energy barrier for this process with different local proton concentrations is only 0.47 eV, which serves as an important factor determining the high-rate performance of the $Zn_{0.5}Mn_2O_4$ cathode. This facile proton transport not only occurs at the boundary between proton-rich and proton-poor regions, but also in the interior of the proton-rich region, as displayed in Figure 4d and Figure S33 (Supporting Information). After the slight adjustment of $-OH$ orientation, the cooperative Grotthuss-type hopping of protons could be easily triggered in a proton-enriched $O^{(1)}$ -tetrahedron, similar to the behavior of collective proton transport in water.^[34,63] We note that with a random distribution of the Zn-vacant sites, the 3D tunnels in spinel structure are essential to offer ample opportunities for the access of proton-poor regions to a nearby proton-rich region where protons could efficiently pass through.

Such a concerted mechanism for proton transport is based on a premise that protons can be dynamically trapped in the $O^{(1)}$ -tetrahedron. To confirm this, we examine the case where two protons are hopping inside an $O^{(1)}$ -tetrahedron (Figure S34, Supporting Information). The energy barrier is 0.22 eV in Grotthuss-type model, remarkably lower than the case (>0.7 eV) where a proton is about to leave the $O^{(1)}$ -tetrahedron heading toward an adjacent $O^{(2)}$ site (Figure S35, Supporting Information). This escape is kinetically accessible only when there are at least four protons in the corresponding $O^{(1)}$ -tetrahedron. Therefore, during their intercalation, protons have a high propensity to be accommodated at the Zn-vacant $O^{(1)}$ -tetrahedron. We further examine the proton transport in Mn_2O_4 , i.e., without Zn^{2+} ions at all $8a$ sites. It is found that neither consecutive hopping mode nor Grotthuss-type concerted hopping mode demonstrates the facile migration of protons (energy barriers are above 1 eV, shown in Figures S36 and S37, Supporting Information). This result underlines the important role of electrostatic interaction between proton-rich and proton-poor regions in facilitating the proton transport in spinel structure. Overall, from the DFT calculations we propose the scenario that proton storage in $Zn_{0.5}Mn_2O_4$ would proceed by preferentially occupying the vacant $8a$ sites, creating proton-rich regions to force the injection of protons to the proton-poor regions, followed by subsequent establishment of interconnected proton-rich regions to permit fast delivery of protons in the entire cathode material.

3. Conclusion

In this study, by taking spinel $ZnMn_2O_4$ as the model system for AZIB cathodes, a defect engineering strategy of Zn deficiency is proposed and the underlying origin of its influence

on proton transport and storage is investigated. Our results demonstrate that the specific capacity of Zn-deficient sample, $Zn_{0.5}Mn_2O_4$, is 33% higher than the near-stoichiometric sample at 0.1C, and more than three times that of the latter at 10C. This superiority can be ascribed to the promotion of reversible proton intercalation, which contributes to more than 90% of the capacity. DFT calculations reveal that the introduction of Zn vacant sites in the lattice leads to the alteration of proton transport behavior from a consecutive single-proton-hopping mode to a concerted Grotthuss-type mode. The latter provides a comprehensive picture that accounts for the accelerated kinetics of proton intercalation, and is corroborated by experimental measurements. Owing to the restricted motion of Zn^{2+} ions, the $Zn_{0.5}Mn_2O_4$ cathode also exhibits extraordinary long-term stability, which underpins the applicability of off-stoichiometry for the facilitation of electrochemical proton storage. We expect that this fresh view of Zn deficiency in modulating proton conduction will guide the design and deployment of manganese oxide cathodes for AZIBs and even for proton batteries in the future.

4. Experimental Section

Material Synthesis: The layered MnO_2 precursors for both near-stoichiometric and Zn-deficient samples were prepared by a microwave assisted hydrothermal method. For the synthesis of near-stoichiometric sample, $KMnO_4$ (6.0 mmol) and $MnSO_4 \cdot H_2O$ (2.0 mmol) were mixed together and dissolved in 35 mL deionized water, while for the synthesis of Zn-deficient sample, $ZnSO_4 \cdot 6H_2O$ (4.0 mmol) was additionally introduced into the above solution. Both solutions were then vigorously stirred at room temperature for 20 min, transferred into a 50 mL microwave hydrothermal device and heated at 160 °C for 2 h. Subsequently, the synthesized powders were collected by filtration and washed with deionized water and absolute ethanol for three times, respectively. The obtained solids were finally dried overnight at 60 °C in vacuum. The as-prepared layered MnO_2 precursors underwent structural transition into spinel phase after electrochemical cycling in an AZIB, during which the pre-inserted Zn^{2+} ions in the layered precursor eventually resulted in Zn deficiency in the bulk of the spinel product. The sintered spinel was prepared by sufficiently mixing $Zn(CH_3COOH)_2$ and $Mn(CH_3COOH)_2$ at the ratio of 1:2, and then calcined at 700 °C in air.

Material Characterization: SEM (ZEISS SUPRA55) and TEM (JEM-3200FS) were used to characterize the morphology and microstructure of the synthesized products and electrodes. XRD (Bruker D8 ADVANCE) measurements with $Cu K\alpha$ radiation were carried out to determine the phase structure of the electrode materials. The atomic ratios of the products and the contents of structural water were evaluated by ICP-OES (JY2000-2) and TGA (SII STA7300 analyzer) measurements, respectively. TGA data were recorded in air using a heating rate of 10 °C min^{-1} from room temperature to 700 °C. XPS (ESCALAB 250Xi) was used to detect the element concentration and electronic structure.

Electrochemical Test: The electrochemical performance of the assembled AZIB was tested in CR2032-type coin cells in air condition. The cathodes were fabricated by mixing active manganese oxide materials, acetylene black (AB) and polyvinylidene fluoride (PVDF) in a weight ratio of 7:2:1, with N-methyl-2-pyrrolidone (NMP) used as a solvent to form a viscous slurry, which was then coated onto a Ti foil. The as-prepared electrodes were cut into disks with the diameter of 10 mm, and then dried in a vacuum oven at about 110 °C for 24 h. The mass loading of the active materials was around 1 mg cm^{-2} . The zinc foil with the diameter of 15 mm and glass fiber membrane were used as anode and separator, respectively, and the aqueous solution containing 3 M $ZnSO_4$ and 0.2 M $MnSO_4$ was used as electrolyte. The LAND-CT2001A

battery-testing instrument was used for electrochemical cycling of the assembled cells. CV and EIS measurements were performed on a Chi 660e electrochemical workstation with potential ranging from 0.95 to 1.85 V versus Zn/Zn²⁺ for CV, and frequency ranging from 100 kHz to 0.1 Hz for EIS.

DFT Calculations: All the DFT calculations were performed using projector augmented wave method as implemented in Vienna ab initio Simulation Package (VASP).^[64–66] The Perdew–Burke–Ernzerhof (PBE)^[67] form of generalized gradient approximation was selected to describe the electronic exchange and correlation. The energy cut-off for structural optimization and static electron energy calculation was 520 eV, with the force converged to 0.01 eV Å⁻¹ and the energy converged to 10⁻⁵ eV. The PBE-U method was adopted, with the Hubbard U parameter of 3.9 eV for Mn so as to take into account the short on-situ Coulomb interaction of the localized 3d electrons.^[68] The Brillouin zone was sampled using the Gamma-centered grid of 3 × 3 × 3. DFT-D3 semi-empirical van der Waals correction was applied to make up for the deficiency of DFT schemes in dealing with dispersion force.^[69] The migration energy barriers of protons and Zn²⁺ ions were calculated using climbing-image nudged elastic band (CI-NEB) method with the force converged to 0.05 eV Å⁻¹.^[70]

Supporting Information

Supporting Information is available from the Wiley Online Library or from the author.

Acknowledgements

R.Q., S.D., and C.H. contributed equally to this work. This work was financially supported by National Natural Science Foundation of China (22109003 and 52102201), Shenzhen Fundamental Research Program (No. GXWD20201231165807007-20200807111854001), Young S&T Talent Training Program of Guangdong Provincial Association for S&T (SKXRC202211), Soft Science Research Project of Guangdong Province (No. 2017B030301013), and the Basic and Applied Basic Research Foundation of Guangdong Province (2022A1515110446).

Conflict of Interest

The authors declare no conflict of interest.

Data Availability Statement

The data that support the findings of this study are available from the corresponding author upon reasonable request.

Keywords

aqueous batteries, concerted proton transport, manganese oxide cathodes, off-stoichiometry, proton storage

Received: November 17, 2022

Revised: March 1, 2023

Published online:

[1] D. Chao, W. Zhou, F. Xie, C. Ye, H. Li, M. Jaroniec, S.-Z. Qiao, *Sci. Adv.* **2019**, *6*, eaba4098.

[2] G. Fang, J. Zhou, A. Pan, S. Liang, *ACS Energy Lett.* **2018**, *3*, 2480.

- [3] B. Tang, L. Shan, S. Liang, J. Zhou, *Environ. Sci.* **2019**, *12*, 3288.
- [4] L. Zhou, L. Liu, Z. Hao, Z. Yan, X.-F. Yu, P. K. Chu, K. Zhang, J. Chen, *Matter* **2021**, *4*, 1252.
- [5] N. Zhang, X. Chen, M. Yu, Z. Niu, F. Cheng, J. Chen, *Chem. Soc. Rev.* **2020**, *49*, 4203.
- [6] M. Chuai, J. Yang, M. Wang, Y. Yuan, Z. Liu, Y. Xu, Y. Yin, J. Sun, X. Zheng, N. Chen, W. Chen, *eScience* **2021**, *1*, 178.
- [7] P. Ruan, S. Liang, B. Lu, H. J. Fan, J. Zhou, *Angew. Chem., Int. Ed.* **2022**, *61*, e202200598.
- [8] R. Qin, Y. Wang, M. Zhang, Y. Wang, S. Ding, A. Song, H. Yi, L. Yang, Y. Song, Y. Cui, J. Liu, Z. Wang, S. Li, Q. Zhao, F. Pan, *Nano Energy* **2021**, *80*, 105478.
- [9] X. Jia, C. Liu, Z. G. Neale, J. Yang, G. Cao, *Chem. Rev.* **2020**, *120*, 7795.
- [10] Q. Zhao, A. Song, S. Ding, R. Qin, Y. Cui, S. Li, F. Pan, *Adv. Mater.* **2022**, *32*, 2002450.
- [11] L. Chen, Q. An, L. Mai, *Adv. Mater. Interfaces* **2019**, *6*, 1900387.
- [12] M. Li, Z. Li, X. Wang, J. Meng, X. Liu, B. Wu, C. Han, L. Mai, *Environ. Sci.* **2021**, *14*, 3796.
- [13] L. E. Blanc, D. Kundu, L. F. Nazar, *Joule* **2020**, *4*, 771.
- [14] G. Liang, F. Mo, X. Ji, C. Zhi, *Nat. Rev. Mater.* **2020**, *6*, 109.
- [15] M. J. Park, H. Y. Asl, A. Manthiram, *ACS Energy Lett.* **2020**, *5*, 2367.
- [16] M. Li, Z. Li, X. Wang, J. Meng, X. Liu, B. Wu, C. Han, L. Mai, *Environ. Sci.* **2021**, *14*, 3796.
- [17] Y. Liu, Z. Qin, X. Yang, J. Liu, X.-X. Liu, X. Sun, *ACS Energy Lett.* **2022**, *7*, 1814.
- [18] Z. Tie, L. Liu, S. Deng, D. Zhao, Z. Niu, *Angew. Chem., Int. Ed.* **2020**, *59*, 4920.
- [19] H. Pan, Y. Shao, P. Yan, Y. Cheng, K. S. Han, Z. Nie, C. Wang, J. Yang, X. Li, P. Bhattacharya, K. T. Mueller, J. Liu, *Nat. Energy* **2016**, *1*, 16039.
- [20] Y. Yuan, R. Sharpe, K. He, C. Li, M. T. Saray, T. Liu, W. Yao, M. Cheng, H. Jin, S. Wang, K. Amine, R. Shahbazian-Yassar, M. S. Islam, J. Lu, *Nat. Sustainability* **2022**, *5*, 890.
- [21] Q. Zhao, A. Song, W. Zhao, R. Qin, S. Ding, X. Chen, Y. Song, L. Yang, H. Lin, S. Li, F. Pan, *Angew. Chem., Int. Ed.* **2020**, *60*, 4169.
- [22] S. Ding, M. Zhang, R. Qin, J. Fang, H. Ren, H. Yi, L. Liu, W. Zhao, Y. Li, L. Yao, S. Li, Q. Zhao, F. Pan, *Nano-Micro Lett.* **2021**, *13*, 173.
- [23] J. Huang, Z. Wang, M. Hou, X. Dong, Y. Liu, Y. Wang, Y. Xia, *Nat. Commun.* **2018**, *9*, 2906.
- [24] C. Xu, B. Li, H. Du, F. Kang, *Angew. Chem., Int. Ed.* **2011**, *51*, 933.
- [25] R. Sun, Q. Liu, W. Deng, *Chin. J. Struct. Chem.* **2022**, *5*, 2205085.
- [26] F. Wan, Z. Niu, *Angew. Chem., Int. Ed.* **2019**, *58*, 16358.
- [27] Q. Zhao, L. Liu, J. Yin, J. Zheng, D. Zhang, J. Chen, L. A. Archer, *Angew. Chem., Int. Ed.* **2020**, *59*, 3048.
- [28] L. Wang, K.-W. Huang, J. Chen, J. Zheng, *Sci. Adv.* **2019**, *5*, eaax4279.
- [29] Z. Yao, Q. Wu, K. Chen, J. Liu, C. Li, *Environ. Sci.* **2020**, *13*, 3149.
- [30] H. Yi, R. Qin, S. Ding, Y. Wang, S. Li, Q. Zhao, F. Pan, *Adv. Funct. Mater.* **2021**, *31*, 2006970.
- [31] Q. Yang, F. Mo, Z. Liu, L. Ma, X. Li, D. Fang, S. Chen, S. Zhang, C. Zhi, *Adv. Mater.* **2019**, *31*, 1901521.
- [32] S. Huang, F. Wan, S. Bi, J. Zhu, Z. Niu, J. Chen, *Angew. Chem., Int. Ed.* **2019**, *58*, 4313.
- [33] Z. Qiu, Y. Fu, M. Chen, J. Zhao, C. Sun, *Chinese J. Struct. Chem.* **2021**, *40*, 1535.
- [34] D. Marx, M. E. Tuckerman, J. Hutter, M. Parrinello, *Nature* **1999**, *397*, 601.
- [35] C. T. Wolke, J. A. Fournier, L. C. Dzigan, M. R. Fagiani, T. T. Odbadrakh, H. Knorke, K. D. Jordan, A. B. McCoy, K. R. Asmis, M. A. Johnson, *Science* **2016**, *354*, 1131.
- [36] K. Xu, *Nat. Energy* **2019**, *4*, 93.
- [37] L. R. Merte, G. Peng, R. Bechstein, F. Rieboldt, C. A. Farberow, L. C. Grabow, W. Kudernatsch, S. Wendt, E. Lægsgaard, M. Mavrikakis, F. Besenbacher, *Science* **2012**, *336*, 889.

- [38] F. Tang, Z. Li, C. Zhang, S. G. Louie, R. Car, D. Y. Qiu, X. Wu, *Proc. Natl. Acad. Sci. USA* **2022**, *119*, e2201258119.
- [39] B. Sambandam, V. Mathew, S. Kim, S. Lee, S. Kim, J. Y. Hwang, H. J. Fan, J. Kim, *Chem* **2022**, *8*, 924.
- [40] N. Zhang, F. Cheng, Y. Liu, Q. Zhao, K. Lei, C. Chen, X. Liu, J. Chen, *J. Am. Chem. Soc.* **2016**, *138*, 12894.
- [41] D. Zhang, J. Cao, X. Zhang, N. Insin, S. Wang, J. Han, Y. Zhao, J. Qin, Y. Huang, *Adv. Funct. Mater.* **2021**, *31*, 2009412.
- [42] S. Deng, Z. Tie, F. Yue, H. Cao, M. Yao, Z. Niu, *Angew. Chem., Int. Ed.* **2022**, *61*, 202115877.
- [43] F. Chen, Q. Wang, X. Yang, C. Wang, H. Zang, Y. Tang, T. Li, B. Geng, *Nano Res.* **2023**, *16*, 1726.
- [44] X. Wu, Y. Xiang, Q. Peng, X. Wu, Y. Li, F. Tang, R. Song, Z. Liu, Z. He, X. Wu, *J. Mater. Chem. A* **2017**, *5*, 17990.
- [45] M. Liu, Z. Rong, R. Malik, P. Canepa, A. Jain, G. Ceder, K. A. Persson, *Environ. Sci.* **2014**, *8*, 964.
- [46] S. Ding, L. Liu, R. Qin, X. Chen, A. Song, J. Li, S. Li, Q. Zhao, F. Pan, *ACS Appl. Mater. Interfaces* **2021**, *13*, 22466.
- [47] H. Zhang, J. Wang, Q. Liu, W. He, Z. Lai, X. Zhang, M. Yu, Y. Tong, X. Lu, *Energy Storage Mater.* **2019**, *21*, 154.
- [48] L. Jiang, Z. Wu, Y. Wang, W. Tian, Z. Yi, C. Cai, Y. Jiang, L. Hu, *ACS Nano* **2019**, *13*, 10376.
- [49] L. Chen, Z. Yang, F. Cui, J. Meng, Y. Jiang, J. Long, X. Zeng, *Mater. Chem. Front.* **2019**, *4*, 213.
- [50] Q. Ye, R. Dong, Z. Xia, G. Chen, H. Wang, G. Tan, L. Jiang, F. Wang, *Electrochim. Acta* **2014**, *141*, 286.
- [51] V. R. Galakhov, M. Demeter, S. Bartkowski, M. Neumann, N. A. Ovechkina, E. Z. Kurmaev, N. I. Lobachevskaya, Ya. M. Mukovskii, J. Mitchell, D. L. Ederer, *Phys. Rev. B* **2002**, *65*, 113102.
- [52] V. P. Santos, M. F. R. Pereira, J. J. M. Órfão, J. L. Figueiredo, *Top. Catal.* **2009**, *52*, 470.
- [53] D. Wang, L.-M. Liu, S.-J. Zhao, B.-H. Li, H. Liu, X.-F. Lang, *Phys. Chem. Chem. Phys.* **2013**, *15*, 9075.
- [54] K. Cai, S. Luo, J. Feng, J. Wang, Y. Zhan, Q. Wang, Y. Zhang, X. Liu, *Chem. Rec.* **2021**, *22*, e202100169.
- [55] Q. Zhao, X. Chen, Z. Wang, L. Yang, R. Qin, J. Yang, Y. Song, S. Ding, M. Weng, W. Huang, J. Liu, W. Zhao, G. Qian, K. Yang, Y. Cui, H. Chen, F. Pan, *Small* **2019**, *15*, 1904545.
- [56] W. Zong, H. Guo, Y. Ouyang, L. Mo, C. Zhou, G. Chao, J. Hofkens, Y. Xu, W. Wang, Y. Miao, G. He, I. P. Parkin, F. Lai, T. Liu, *Adv. Funct. Mater.* **2022**, *32*, 2110016.
- [57] W. Zong, N. Chui, Z. Tian, Y. Li, C. Yang, D. Rao, W. Wang, J. Huang, J. Wang, F. Lai, T. Liu, *Adv. Sci.* **2021**, *8*, 2004142.
- [58] S. Zhu, Y. Dai, J. Li, C. Ye, W. Zhou, R. Yu, X. Liao, J. Li, W. Zhang, W. Zong, R. Chen, G. He, D. Chao, Q. An, *Sci. Bull.* **2022**, *67*, 1882.
- [59] Y. Wang, C. Chen, H. Ren, R. Qin, H. Yi, S. Ding, Y. Li, L. Yao, S. Li, Q. Zhao, F. Pan, *Sci. China Mater.* **2021**, *65*, 78.
- [60] H. Yi, C. Zuo, H. Ren, W. Zhao, Y. Wang, S. Ding, Y. Li, R. Qin, L. Zhou, L. Yao, S. Li, Q. Zhao, F. Pan, *Nanoscale* **2021**, *13*, 14408.
- [61] W. Pan, J. Mao, Y. Wang, X. Zhao, K. W. Leong, S. Luo, Y. Chen, D. Y. C. Leung, *Small Methods* **2021**, *5*, 2100491.
- [62] X. Zeng, J. Liu, J. Mao, J. Hao, Z. Wang, S. Zhou, C. D. Ling, Z. Guo, *Adv. Energy Mater.* **2020**, *10*, 904163.
- [63] Y. Tian, J. Hong, D. Cao, S. You, Y. Song, B. Cheng, Z. Wang, D. Guan, X. Liu, Z. Zhao, X.-Z. Li, L.-M. Xu, J. Guo, J. Chen, E.-G. Wang, Y. Jiang, *Science* **2022**, *377*, 315.
- [64] G. Kresse, J. Hafner, *Phys. Rev. B: Condens. Matter* **1993**, *47*, 558.
- [65] G. Kresse, J. Furthmüller, *Phys. Rev. B* **1996**, *54*, 11169.
- [66] G. Kresse, D. Joubert, *Phys. Rev. B* **1998**, *59*, 1758.
- [67] J. P. Perdew, K. Burke, M. Ernzerhof, *Phys. Rev. Lett.* **1996**, *77*, 3865.
- [68] S. L. Dudarev, G. A. Botton, S. Y. Savrasov, C. J. Humphreys, A. P. Sutton, *Phys. Rev. B* **1998**, *57*, 1505.
- [69] S. Grimme, J. Antony, S. Ehrlich, H. Krieg, *J. Chem. Phys.* **2010**, *132*, 154104.
- [70] G. Henkelman, B. P. Uberuaga, H. Jónsson, *J. Chem. Phys.* **2000**, *113*, 9901.